UC Berkeley
SEMM Reports Series

Title

A Local Integration Method for Coupled Damage and Plasticity

Permalink

https://escholarship.org/uc/item/9mm3q68r

Authors

Govindjee, Sanjay

Hall, Garrett

Publication Date

1998

A Local Integration Method for Coupled Damage and Plasticity

Sanjay Govindjee

Garrett Hall

Structural Engineering Mechanics and Materials

Department of Civil and Environmental Engineering,

University of California

Berkeley, CA 94720-1710

Abstract

A solution algorithm for solving the local equations of state in a coupled damage and plasticity model is investigated and applied to the specific problem of concrete. The proposed algorithm algorithm is based on a quasi-Newton method that decouples the damage from the plasticity. This technique avoids problems associated with the coupling terms and produces a robust local constitutive integration methodology. Numerical examples are provided to illustrate the behavior of the proposed method.

1

1   Introduction

The analysis of concrete behavior through the use of continuum models has been treated extensively in the literature. The vast majority of modeling approaches, whether motivated by direct consideration of micromechanical mechanisms (e.g. Ortiz [8]), dissipative energy based approaches (e.g. Ju [2], Govindjee et. al. [1]), or direct observation of macroscopic test results, invariably include both damage and plasticity. More often than not, these mechanisms are postulated to be coupled (e.g. Han and Chen [6]) based on both theoretical and observed behaviors. Such coupling gives rise to a set of equations similar to those of multisurface plasticity, with the additional complication that the surfaces may evolve even when inactive.

The basic computational methodology for treating multisurface plasticity was laid out by Simo et. al. [18]. This methodology, however, while formally correct often produces a local return map problem that is virtually intractable for general strain time histories. For this reason researchers have sought alternative numerical methods such as the "operator split" method for explicit calculations of Ju and Simo [20]. However, such methodologies can show pathological behavior in general implicit computations and further often lead to unsymmetric tangents. The primary goal of the present work is to develop a robust local integration methodology for combined plasticity and damage that is applicable to implicit computations and retains symmetric tangent operators when appropriate. The important and difficult issue of global integration methodologies for damage systems is not addressed.

To provide a specific context for the work, we look at the model of Govindjee et. al. [1] and augment it with a Drucker-Prager plasticity constraint. The base model is a smeared crack type model (Rashid [16]) that utilizes the stiffness/compliance of the system as an internal variable, similar to Ortiz's model [8]. Energy regularization is achieved through a modification of Oliver's technique [15]. History variables in the model keep track of crack orientation and intensity. The crack orientation is initialized by introducing crack surfaces in stress space when a tensile cut-off is exceeded (see Figure 1). Each crack may be interpreted as five constraint surfaces in stress space; one representing tension across the crack, and four representing reduced shear capacity across the crack surface. The evolution of these surfaces are related to the material compliance through the postulate of maximum dissipation.

An outline of the paper is as follows: In Section 2 the constitutive equations of the model are briefly reviewed, followed in Section 3 by a presentation of the proposed algorithm. Section 4 discusses several pertinent algorithmic issues and Section 5 provides several illustrative examples.

2 Summary of the Model

Consider a body occupying the region $\Omega \subset \Re^3$ comprised of the material of interest. Restricting the strain tensor to be that of the infinitesimal theory (see Remark 3.3), each point in the continuum is assumed to obey the relation:

$$\boldsymbol{\sigma} = \mathcal{C} : (\boldsymbol{\varepsilon} - \boldsymbol{\varepsilon}_p) \tag{1}$$

where $\boldsymbol{\sigma}$ is the stress, $\boldsymbol{\varepsilon}$ is the strain, $\boldsymbol{\varepsilon}_p$ is the plastic strain, and $\mathcal{C}$ is the rank four stiffness tensor. For later use we define the compliance $\mathcal{D} = \mathcal{C}^{-1}$. The space of admissible stress states are constrained by the functions $\phi_k \in \Phi$

$$\phi_1 = \mathbf{H}_1 : \boldsymbol{\sigma} - f_n + k_n q_d \le 0 \tag{2}$$

$$\phi_2 = |\mathbf{H}_2 : \boldsymbol{\sigma}| - f_s + k_s q_d \le 0 \tag{3}$$

$$\phi_3 = |\mathbf{H}_3 : \boldsymbol{\sigma}| - f_s + k_s q_d \le 0 \tag{4}$$

$$\phi_4 = \|\mathcal{P} : \boldsymbol{\sigma}\| + \beta \boldsymbol{\sigma} : \mathbf{I} + q_p \le 0 \tag{5}$$

thereby restricting the elastic domain to

$$\mathbf{E}_\sigma = \{\boldsymbol{\tau} \in \mathbf{S} \mid \phi_k(\boldsymbol{\tau}, q_d, q_p) \le 0 \quad (k = 1, \ldots, 4)\} \tag{6}$$

Here, q_d and q_p are "hardening" functions of the internal variables α_d and α_p which are related to the evolution of brittle damage and plasticity, respectively. $\mathbf{S}$ is the set of all symmetric rank two tensors, $\mathcal{P}$ is the deviatoric projector, $\mathbf{I}$ is the rank two identity, and the terms $\mathbf{H}_i$ are defined as

$$\mathbf{H}_1 = \mathbf{n} \otimes \mathbf{n} \tag{7}$$

$$\mathbf{H}_2 = \frac{1}{2}(\mathbf{n} \otimes \mathbf{m} + \mathbf{m} \otimes \mathbf{n}) \tag{8}$$

$$\mathbf{H}_3 = \frac{1}{2}(\mathbf{n} \otimes \mathbf{l} + \mathbf{l} \otimes \mathbf{n}) \tag{9}$$

This formulation is based upon a crack orientation with $\mathbf{n}$ as a normal, and $\mathbf{m}, \mathbf{l}$ forming an orthonormal basis in the plane of the crack. With this construction, the double contraction $\mathbf{H}_1 : \boldsymbol{\sigma}$ determines the normal stress across the crack, while $\mathbf{H}_2$ and $\mathbf{H}_3$ single out shear stresses acting across the crack plane. The parameters f_n and f_s denote critical normal and shear stress values. k_n and k_s are coupling constants linking degradation between shear and tensile surfaces, and β is the pressure coefficient for the plasticity surface.

3

The evolution of the internal variables governing both damage and plasticity are dictated by flow rules derived from a dissipation argument:

$$\dot{\mathcal{D}} = \gamma_1 \frac{\partial_\sigma \phi_1 \otimes \partial_\sigma \phi_1}{\partial_\sigma \phi_1 : \boldsymbol{\sigma}} + \gamma_2 \frac{\partial_\sigma \phi_2 \otimes \partial_\sigma \phi_2}{\partial_\sigma \phi_2 : \boldsymbol{\sigma}} + \gamma_3 \frac{\partial_\sigma \phi_3 \otimes \partial_\sigma \phi_3}{\partial_\sigma \phi_3 : \boldsymbol{\sigma}} \tag{10}$$

$$\dot{\boldsymbol{\varepsilon}}_p = \gamma_4 \partial_\sigma \phi_4 \tag{11}$$

$$\dot{\alpha}_d = \gamma_1 \frac{\partial \phi_1}{\partial q_d} + \gamma_2 \frac{\partial \phi_2}{\partial q_d} + \gamma_3 \frac{\partial \phi_3}{\partial q_d} \tag{12}$$

$$\dot{\alpha}_p = \gamma_4 \frac{\partial \phi_4}{\partial q_p} \tag{13}$$

These flow rules simply correspond to associated damage and plasticity. The consistency parameters $\gamma_k, (k = 1, \ldots 4)$ are determined from loading and unloading conditions of the Kuhn-Tucker type; viz.

$$\phi_k (\boldsymbol{\sigma}, q_d, q_p) \le 0 \quad , \quad \gamma_k \ge 0 \quad , \quad \phi_k (\boldsymbol{\sigma}, q_d, q_p) \, \gamma_k = 0 \tag{14}$$

to which the consistency condition is added:

$$\dot{\phi}_k (\boldsymbol{\sigma}, q_d, q_p) \, \gamma_k = 0 \tag{15}$$

Reasonable choices for the functions q_d and q_p are:

$$q_d = f_n (1 - exp[-g\alpha_d]) \tag{16}$$

$$q_p = -\sigma_y - k\alpha_p \tag{17}$$

where g, σ_y, and k are additional constitutive parameters.

We next consider a time integrated form of the continuous equations presented above. To integrate the constitution from a time t_n to a time $t_{n+1} = t_n + \Delta t$, $\Delta t > 0$, we apply a backward Euler method to flow rules (10) through (13). Denoting by $\Delta \gamma_k = \gamma_k \Delta t$, we have

$$\mathcal{D}^{n+1} = \mathcal{D}^n + \sum_{k=1}^{3} \Delta \gamma_k \frac{\partial_\sigma \phi_k^{n+1} \otimes \partial_\sigma \phi_k^{n+1}}{\partial_\sigma \phi_k^{n+1} : \boldsymbol{\sigma}^{n+1}} \tag{18}$$

$$\boldsymbol{\varepsilon}_p^{n+1} = \boldsymbol{\varepsilon}_p^n + \Delta \gamma_4 \partial_{q_p} \phi_4^{n+1} \tag{19}$$

$$\alpha_d^{n+1} = \alpha_d^n + \Delta \gamma_1 \partial_{q_d} \phi_1^{n+1} + \Delta \gamma_2 \partial_{q_d} \phi_2^{n+1} + \Delta \gamma_3 \partial_{q_d} \phi_3^{n+1} \tag{20}$$

$$\alpha_p^{n+1} = \alpha_p^n + \Delta \gamma_4 \partial_{q_p} \phi_4^{n+1} \tag{21}$$

where superscripts "n" and "$n+1$" indicate functions evaluated at time t_n and t_{n+1}. The stress at time t^{n+1} can be expressed as

$$\boldsymbol{\sigma}^{n+1} = \mathcal{C}^n : \{\boldsymbol{\varepsilon}^{n+1} - \boldsymbol{\varepsilon}_p^n - \sum_{k=1}^{3} \Delta \gamma_k \partial_\sigma \phi_k^{n+1}\} \tag{22}$$

Remark 2.1 The above discrete equations are viewed as strain driven; i.e. it is assumed that ε^{n+1} is known and the objective is to solve these algebraic equations for σ^{n+1}, $\mathcal{C}^{n+1} = (\mathcal{D}^{n+1})^{-1}$, ε_p^{n+1}, α_p^{n+1}, and α_d^{n+1}. Further, the Kuhn Tucker conditions are assumed to be enforced at time t_{n+1} during this process.

Remark 2.2 The incompatibility between dissipation per unit volume, as implied above, and the physical mechanism of crack growth is treated by introduction of a length scale; see [1] for details.

Remark 2.3 Rate dependency may be incorporated into the evolution by replacing each $\Delta\gamma_k$ with $\frac{<\phi_k>\Delta t}{\eta}$. This requires no modifications to the solution algorithm shown below; see [1] or [18] for further discussion on this point.

Remark 2.4 With the framework outlined above, this multisurface problem is complicated by the fact that the damage equations are coupled via α_d (Eq. 12), and thus evolution occurs on surfaces which are not currently active. This, combined with the softening/hardening rules, makes it difficult to determine apriori the active set of constraints which are consistent with the model; see [18]. The algorithmic treatment in the following section is motivated by this difficulty.

3 Solution Methodology

3.1 Solution of Coupled Evolution Equations

The fundamental difficulty in solving the set of nonlinear algebraic time discretized equations presented in the previous section lies in the determination of the correct set of active surfaces. Although this problem exists and has been treated in general multisurface plasticity [18], here it is complicated by the fact that even inactive surfaces may evolve due to coupling with active surfaces. Analysis of a similar problem has been presented in the work of Ju and Simo [20], where an algorithm is derived from the successive solution of subproblems arrived at by an additive split of the stress tensor into damage and plasticity parts. Although this algorithm had the computational disadvantage of an unsymmetric tangent, later work by Ju [2] amended the approach based on a three part strain operator split consisting of elastic, plastic and damage components which when added are consistent with the full problem. This approach had the advantage that although the tangent modulus was in general unsymmetric, for typical models (e.g. J_2 plasticity) a symmetric tangent was recovered.

The method presented in this paper, although it does not employ an explicit split of the stress or strain tensors, is similar in that solutions of the damage and plasticity surfaces remain uncoupled within the algorithm, thereby resulting in a simplified implementation. This is achieved through the use of a quasi–Newton iteration which not only maximizes code reuse, but is nearly as efficient as a full iteration in this particular application. Further, the full set of algebraic equations are simultaneously satisfied at the end of the time step; this does not occur in the "operator split" methods mentioned above. With the handling of pathological cases which may arise (Section 4), the method is shown in Section 5 to be a reasonable approach to solving the local constitutive equations for what are traditionally difficult analysis problems.

In all of what follows, it is assumed that the model is to be implemented within the traditional strain driven finite element framework. As such, the constitutive model discussed herein may be envisaged to exist at a single Gauss point within an unspecified array of integration points. Further consideration of a specific global problem is not necessary at this point.

3.2 Return Mapping Algorithm

Given the model outlined thus far, we begin by considering a solution strategy based on classical return mapping algorithms comprised of an elastic predictor, and in this case, both damage and plasticity correctors. A summary flow chart of the entire algorithm is shown in Figure 2. The algorithm is initialized with a trial stress based on the assumption that the incremental strain is fully elastic.

$$\boldsymbol{\sigma}_{trial}^{n+1} = \mathcal{C}^n : \left\{ \boldsymbol{\varepsilon}^{n+1} - \boldsymbol{\varepsilon}_p^n \right\} = \boldsymbol{\sigma}^n + \mathcal{C}^n : \Delta \boldsymbol{\varepsilon}^n \tag{23}$$

The remaining variables are initialized based on previous values.

$$q_{d-trial}^{n+1} = q_d^n = q_d(\alpha_d^n) \tag{24}$$

$$q_{p-trial}^{n+1} = q_p^n = q_p(\alpha_p^n) \tag{25}$$

After initialization, a check is made of all ϕ_k surfaces to determine if the stress is in the elastic domain. If this is so, the final stress is the correct solution, and all evolution variables are updated to t^{n+1}. However, if any of the surfaces have been violated, they are assumed for the time being to belong to the active set of equations, and a solution of these equations must be pursued. These steps are summarized in Algorithm Part 1.

Algorithm Part 1 Return Mapping Algorithm Set Up:

1. Given strain at time t^{n+1}:

$$\varepsilon^{n+1} = \varepsilon^n + \Delta\varepsilon \tag{26}$$

2. Compute trial stress:

$$\sigma_{trial}^{n+1} = \sigma^n + \mathcal{C}^n : \Delta\varepsilon \tag{27}$$

3. Compute trial surface functional values:

$$\phi_k = \phi_k\left(\sigma_{trial}^{n+1}, q_d^n, q_p^n\right) \tag{28}$$

4. Determine active surface list:

$$s_{active}^{trial} = s_d^{trial} + s_p^{trial} \tag{29}$$

$$s_d^{trial} = \{\alpha \in \{1,2,3\} \mid \phi_\alpha\left(\sigma_{trial}^{n+1}, q_d^n\right) > 0\} \tag{30}$$

$$s_p^{trial} = \{\alpha \in \{4\} \mid \phi_\alpha\left(\sigma_{trial}^{n+1}, q_p^n\right) > 0\} \tag{31}$$

5. IF $s_{active} = \emptyset$ THEN

$$\sigma^{n+1} = \sigma_{trial}^{n+1} \tag{32}$$

$$\mathcal{D}^{n+1} = \mathcal{D}^n \tag{33}$$

$$q_d^{n+1} = q_d^n \tag{34}$$

$$q_p^{n+1} = q_p^n \tag{35}$$

$$\tag{36}$$

ELSE GOTO Algorithm Part 2

6. Update history: END

3.3   Determination and Solution of Active Equations

We now consider finding a solution when $s_{active} \neq \emptyset$. The procedure, which is outlined below, first solves for the consistency parameters of the current active set s_{active}. This is done using a quasi–Newton algorithm whereby the stress state is updated after each subsequent solution involving either the coupled damage surfaces or the plasticity surface. During this part of the solution, it is possible to determine if a surface should be dropped from the active set by the sign of its associated consistency parameter. As discussed in [18], the equations which have a negative consistency parameter do not belong to the

active set (as dictated by the loading/unloading conditions) and must be removed from s_{active} and the return map equations solved again, i.e. one must iterate in general.

Once convergence is achieved on s_{active} with a corresponding set of positive $\Delta\gamma_k$, the yield functions must be checked against this final state to determine if any surfaces, during the evolution of the elastic domain, were violated. Should this occur, it indicates that the currently active set is incomplete, and the solution is iterated upon again with the necessary equations flagged as active. The process repeats until the active set of equations satisfies all of the loading and consistency conditions. This procedure is summarized in Algorithm Part 2.

Algorithm Part 2 Multi-Surface Algorithm

1. Initialize active set and trial stress; the iteration counter is initialized to one ($i = 1$).

$$s_{active}^i = s_d^i + s_p^i \tag{37}$$
$$\boldsymbol{\sigma}^i = \boldsymbol{\sigma}_{trial}^{n+1} \tag{38}$$
$$q_d^i = q_{d-trial}^{n+1} \tag{39}$$
$$q_p^i = q_{p-trial}^{n+1} \tag{40}$$

2. IF $s_d \neq \emptyset$ AND $s_p = \emptyset$; solve damage equations with a full newton method to produce new iterate; see [1],

$$q_d^i \rightarrow q_d^{i+1} \tag{41}$$
$$\boldsymbol{\sigma}^i \rightarrow \boldsymbol{\sigma}^{i+1} = \boldsymbol{\sigma}^i - \mathcal{C}^n : \Delta\gamma_k \partial_\sigma \phi_k \quad \forall k \in s_d^i \tag{42}$$

ELSE IF $s_p \neq \emptyset$ AND $s_d = \emptyset$; solve plasticity using a full newton method to produce new iterate; see [7]

$$q_p^i \rightarrow q_p^{i+1} \tag{43}$$
$$\boldsymbol{\sigma}^i \cdot \rightarrow \boldsymbol{\sigma}^{i+1} = \boldsymbol{\sigma}^i - \mathcal{C}^n : \Delta\gamma_k \partial_\sigma \phi_k \quad \forall k \in s_p^i \tag{44}$$

ELSE IF $s_d^i \neq \emptyset$ AND $s_p^i \neq \emptyset$: GOTO Algorithm 3

3. Update active surface list:

$$s_{active}^{i+1} = \{\alpha \mid \Delta\gamma_\alpha \geq 0\} \tag{45}$$

4. IF $s_{active}^{i+1} \neq s_{active}^i$ THEN $i = i + 1$, GOTO 2 and resolve with new active set.

5. Check inactive surfaces:

$$s^* = \left\{ \alpha \notin s^i_{active} \mid \phi_\alpha \left(\boldsymbol{\sigma}^{i+1}, q_d^{i+1}, q_p^{i+1} \right) \geq 0 \right\} \tag{46}$$

6. IF $s^* \neq \emptyset$ THEN

$$s^{i+1}_{active} = \{s^i_{active}, s^*\} \tag{47}$$
$$i = i + 1 \tag{48}$$

   GOTO 2 and resolve with new active set.

7. Converged solution, update and return:

$$\boldsymbol{\sigma}^{n+1} = \boldsymbol{\sigma}^{i+1} \tag{49}$$
$$q_d^{n+1} = q_d^{i+1} \tag{50}$$
$$q_p^{n+1} = q_p^{i+1} \tag{51}$$

The procedure outlined in Algorithm 3 below treats the case when damage and plasticity surfaces are simultaneously active. By uncoupling damage and plasticity iterations, the same code that is employed in Step 2 Algorithm Part 2 may be reused. The behavior of this iteration technique is discussed in Section 4.

Algorithm Part 3 Algorithm for Simultaneous Damage and Plasticity

1. Initialize given active set and current iterate; the sub-iteration counter is initialized to one ($j = 1$). :

$$s^i_{active} = s^i_d + s^i_p \tag{52}$$
$$\boldsymbol{\sigma}^j = \boldsymbol{\sigma}^i \tag{53}$$
$$q_d^j = q_d^i \tag{54}$$
$$q_p^j = q_p^i \tag{55}$$

2. Solve damage equations with full newton assuming fixed plasticity:

$$q_d^j \rightarrow q_d^{j+1} \tag{56}$$
$$\boldsymbol{\sigma}^j \rightarrow \boldsymbol{\sigma}^{j+} = \boldsymbol{\sigma}^j - \mathcal{C}^n : \Delta\gamma_k \partial_\sigma \phi_k \quad \forall k \in s^i_d \tag{57}$$

9

3. Solve plasticity equations with full newton assuming fixed damage:

$$q_p^j \quad \rightarrow \quad q_p^{j+1} \tag{58}$$

$$\boldsymbol{\sigma}^{j+} \quad \rightarrow \quad \boldsymbol{\sigma}^{j+1} = \boldsymbol{\sigma}^{j+} - \mathcal{C}^n : \Delta\gamma_k \partial_\sigma \phi_k \quad \forall k \in s_p^i \tag{59}$$

4. IF

$$\left| |\Delta\gamma_k^{j+1}| - |\Delta\gamma_k^j| \right| \leq tol_k \quad \forall k \in s_{active}^i \tag{60}$$

THEN Update and RETURN

$$q_p^{i+1} \;=\; q_p^{j+1} \tag{61}$$

$$q_d^{i+1} \;=\; q_d^{j+1} \tag{62}$$

$$\boldsymbol{\sigma}^{i+1} \;=\; \boldsymbol{\sigma}^{j+1} \tag{63}$$

ELSE GOTO 2 and resolve.

Remark 3.1 Since the solution for the consistency variables $\Delta\gamma_k$ occurs exclusively on either the plasticity or damage surfaces at any one time, solution techniques which have been presented previously in the literature (see [1] and [7]) may be used. This approach reduces the problem to a root finding exercise for the scalar damage parameters. The details of this procedure have been left out and are indicated by an arrow ($\rightarrow$) in the algorithms given above.

Remark 3.2 The pressure dependence of the plastic yield function combined with the anisotropic nature of the compliance tensor following crack development complicates the solution for the plastic consistency variable. In contrast to classical J_2 plasticity with linear hardening and a constant isotropic linear elasticity compliance, the scalar equation for the consistency variable can not be reduced to a linear form. Rather, the resulting scalar equation is nonlinear in $\Delta\gamma$ and admits the possibility that no real solution may exist. Such instances are discussed in Section 4.5.

Remark 3.3 While the modeling of brittle materials does not generally require a large strain model, it may be desirable to remove stresses induced by large rigid deformations. The current model may be modified for this possibility by replacing $\boldsymbol{\varepsilon}$ with the Green-Lagrange strain measure $\boldsymbol{E}$ and $\boldsymbol{\sigma}$ with the Second Piola-Kirchhoff stress measure $\boldsymbol{S}$. The

10

pertinent modifications are then given by:

$$E = \frac{1}{2}\{\nabla u + \nabla u^T + \nabla u^T \nabla u\} \tag{64}$$

$$S = \mathcal{C} : \{E - E_p\} \tag{65}$$

Oliver's length scale is computed in the reference domain and the only other modifications required are to add geometric terms to the tangent.

Remark 3.4 In typical finite element applications it is advantageous to have the algorithmic tangent of the material model available as opposed to the continuum tangent [19]. For completeness, the consistent tangent for the general case (including rate dependent damage surfaces) is included in Appendix A.

4 Computational Issues

In this section a number of small examples are examined which demonstrate specific behavioral aspects of the proposed algorithm. This endeavor is aided by a graphical interpretation which provides insight into the physical behavior of the model under consideration.

4.1 State Determination: Graphical Interpretation

As mentioned in [18], yield functions based on stress or strain may be considered as surfaces in a rank two tensor space. Symmetry of these tensors reduces the number of independent dimensions to six. However, considering the "hardening" parameters as evolution variables, additional dimensions are gained (q_p, q_d). Figure 3 shows the nonsmooth surface intersections in a subspace of these multiple dimensions.

If one considers multisurface perfect plasticity, it is known that for two surfaces to be simultaneously active, the trial state must lie in the cone formed by the normals to the two surfaces. For the equations considered here, the possibility of a solution based solely on a geometric construction is clouded by the coupling through the hardening/softening terms. This coupling can reduce the requirement that the trial state lie in a normal cone from a necessary condition to a sufficient one for activation of the surfaces forming the cone. To demonstrate, a specific problem is considered next.

By reducing the dimensions of the problem through consideration of a purely planar stress state, the advantages of simplicity are gained without loss of generality. To this

end, a typical problem involving two surfaces may be defined by the equations

$$\phi_1 = \mathbf{H}_1 : \boldsymbol{\sigma} - f_n + k_n f_n (1 - \exp(-g\alpha_d))$$
$$\phi_4 = \|\mathcal{P} : \boldsymbol{\sigma}\| + \beta \boldsymbol{\sigma} : \mathbf{I} - \sigma_y - k\alpha_p$$

where

$$
\begin{aligned}
f_n &= 400 \\
k_n &\approx 1 \\
g &= 1632 \\
\beta &= 0.1 \\
\sigma_y &= 1000 \\
k &= -500000
\end{aligned}
$$

A graphical representation is given in Figure 4; the normals to each surface have been indicated at one of the points where they intersect. As is apparent from the illustration, a large portion of the plasticity surface is separated from the elastic domain by the tensile limit of the material. This creates the interesting problem of state determination in the six regions surrounding the intersection (where four of these regions indicate activation of at least one constraint). In the following subsections, load paths are considered which drive the stress state through the different regions. This serves as a means to illustrate the behavior of the proposed algorithm.

4.2 Reduction of Active Set

We first consider two examples of how surfaces may be removed from the active set. For this purpose, consider $s_{active}^{trial} = \{\phi_1, \phi_4\}$ where both surfaces exhibit softening (the specific regions of interest are two and four as labeled in Figure 4). The simultaneous solution for the active set, as arrived at by Algorithm Part 3 is given by the dashed lines in Figures 5 and 6. In both cases, the final value of one of the consistency variables is less than zero in violation of the Kuhn-Tucker conditions. From the plots it is apparent that these solutions correspond to physically unrealistic behavior. By removing the corresponding ϕ from s_{active}, the correct solution involving only a single surface is subsequently obtained. Note that since these two surfaces are not coupled, the active set may have been inferred apriori based on the normals (see [18]).

12

4.3 Corner Solution

Again referring to Figure 4, assume the trial stress state is now in the normal cone formed by ϕ_1 and ϕ_4. In this case the initial active set is the correct one, and a solution satisfying both the damage and plasticity equations is readily obtained; see Figure 7. The convergence behavior for this quasi-Newton iteration, specifically when damage and plasticity surfaces are both active, is observed to be linear. Remark 4.1 discusses the frequency with which such solutions are actually observed.

4.4 Evolution of Inactive Surfaces

Demonstration of the need for Step 7 in Algorithm 2, which checks the condition of inactive surfaces at a potential solution point, is given graphically in Figures 8 (a) and 8 (b). The first figure shows the trial state in relation to the elastic domain defined by surfaces ϕ_1 and ϕ_2, where it is clear that the active set would be initialized as ϕ_1 only. The next graphic shows the return map path ($\leftarrow$) and the final surfaces with softening (dashed lines) resulting in violation of ϕ_2 at the proposed solution. By adding surface two into the active set, the correct solution is found. This portion of the algorithm plays a significant role in the analysis of the plain notched concrete beam of Section 5.1.

4.5 Pathological Cases

To improve the stability of the algorithm in the presence of poor conditioning (which, as an example, may arise after significant material degradation due to cracking), the handling of certain pathological cases has been included in the subroutines solving for the consistency parameters. More specifically, the determination of a lack of solution in any subroutine is not considered as cause for failure, rather, the corresponding surface is dropped from the active set, and a solution is pursued with the remaining surfaces. This is equivalent to setting the consistency variable of a surface which did not converge locally to a negative value and continuing as normal. If a solution is then found which satisfies all of the loading/unloading/consistency conditions for every surface, the standard solution continues. Note that after sufficient damage has occurred in the material, the elastic domain becomes severely restricted and the system as a whole becomes more nearly singular. In such cases, it has been observed that it is possible to reach a state to which no solution to the local constitutive equations can be found algorithmically.

Remark 4.1 The frequency with which various solution branches are called upon during a solution is necessarily affected by the physics of the problem being solved as well as

the shapes of the surfaces themselves. However, for any given set of yield functions and problem, the step size (i.e. load increment) has a significant affect on the number of iterations spent trying to determine the active set. The further a given trial state is from the elastic domain, the less likely the initial set will bear any resemblance to the final active set. At the other end of the spectrum, very small load steps recover what is essentially an event to event algorithm where the initial set is (in the limit) always the correct set. In this case the likelihood of the load path going exactly through one of the non-smooth intersection points of the elastic domain surface is extremely small.

Remark 4.2 The previous examples have linear convergence when both damage and plasticity surfaces belong to the active set. This is to be expected, considering the uncoupled approach which has been taken. Based on the examples in the final section, and in light of Remark 4.1, this slight loss in numerical efficiency is acceptable given the adaptability of the algorithm.

5 Applications

This final section demonstrates the utility of the model presented herein by comparing the model against experimental data involving plain concrete as well as steel reinforced concrete. All calculations were performed using the finite element code FEAP developed at the University of California.

5.1 Numerical Examples

The following examples are drawn from [1] with the intention of testing the local constitutive algorithm in realistic problems.

Plain Notched Concrete Beam

The first problem considered is that of a plain notched concrete beam in three point bending. The original experiment was performed by Malvar [17] on a beam measuring four by four by 31 inches (depth, width and height). The mesh used in the analysis presented here employed quarter symmetry with a notch of one half inch extending halfway through the depth of the beam. The constitutive parameters for the concrete were set to $E = 3.15 \times 10^6 psi$, $f_n = 449.6 psi$, $G_f = .436 lbs/in$, $\nu = 0.2$, $f_s = 2103 psi$, $\beta_s = 0.03$, $\eta = 0.001 psi - sec$, $f_c^i = 4206 psi$, $\beta_p = 0.1$, and $k = -1/2 \times 10^6$. The centerline of the beam was driven to a displacement of $0.035 in$, with the results shown in Figure 9.

14

This particular example is relevant in that following the attainment of peak strength, the activation of shear surfaces which were not initially in s^i_{trial} occurred regularly (through the coupling terms on the shear and tensile surfaces, as illustrated in Figure 8). This continued until the material had shed approximately half its maximum load, at which point the elastic region had shrunk (thereby increasing the size of the normal cone) sufficiently to avoid this behavior. Towards the end of the run, the poor bending behavior of the eight node bricks becomes apparent.

Reinforced Concrete Beam

The second example is a moderately reinforced concrete beam in three point bending. The beam measures 20 by 8 by 144 inches (depth, width and height), although it was modeled in one quarter symmetry. The tension steel is located 5 inches apart (centered) with two inch cover. It was modeled using classical one dimensional plasticity with the parameters $E = 29.5 \times 10^6 psi$, $\sigma_y = 44.9 \times 10^3 psi$, $A = 0.785 in^2$, and $H = 27.0 \times 10^3 psi$. The constitutive parameters for the concrete were set to $E = 3.5 \times 10^6 psi$, $f_n = 350 psi$, $G_f = 1.0 lbs/in$, $\nu = 0.2$, $f_s = 1750 psi$, $\beta_s = 0.05$, $\eta = 0.001 psi - sec$, $f'_c = 4820 psi$, $\beta_p = 0.1$, and $k = -1 \times 10^6$. The original experiment data is from Burns and Seiss [3].

With the inclusion of reinforcing steel, all parts of the algorithm presented in Section 3 were tested, with the results shown in Figure 10. Also shown is the contribution of the shear surfaces to the material degradation, where it can be seen that without activation of the shear surfaces, the response is grossly overestimated. Despite extensive damage in the concrete, the local algorithm encountered no difficulty in obtaining a solution to the constitutive equations at every iteration.

Heavily Reinforced Concrete Beam

The final problem produced the most diffuse damage pattern of the calculations, and thus serves as an extreme test of the local integration algorithm. In this case, the beam measures 21.75 by 12 by 144 inches (depth, width and height). The two layers of tension steel (two #9 bars in each layer) are located with 2.5 and 5 inch covers and are centered at 7 inches apart. The compression steel (two #4 bars) line up above the tension steel with a cover of two inches from the top of the beam. The material model used for each type of steel is shown in Figure 11. The concrete parameters were set to $E = 3.4 \times 10^6 psi$, $f_n = 350 psi$, $G_f = 4.0 lbs/in$, $\nu = 0.167$, $f_s = 1750 psi$, $\beta_s = 0.05$, $\eta = 0.001 psi - sec$, $f'_c = 3490 psi$, $\beta_p = 0.01$, and $k = -1 \times 10^6$. The original experiment data shown in Figures 11 and 12 is from [9].

The overall response turns out to be controlled by bond slip between the rebar and

the concrete, which explains the calculation's divergence from the experimental data beyond the point shown. Regardless, the problem provides a significant test for the local constitutive algorithm, which never failed to converge.

6 Closure

An integration algorithm for the solution of the local constitutive equations in a coupled damage and plasticity model has been presented and tested in a number of numerical examples which demonstrate its behavior. The algorithm, when embedded in the concrete model presented herein, has been shown to be adequately robust at the local level. However, it is noted that the local convergence is unrelated to the well known difficulty of achieving global convergence for this class of problems.

References

[1] Govindjee, Kay, and Simo, *Anisotropic Modeling and Numerical Simulation of Brittle Damage in Concrete*, International Journal for Numerical Methods in Engineering, Vol. 38, 3611-3633, 1995.

[2] Ju, J.W., *On Energy Based Elastoplastic Damage Theories: Constitutive Modeling and Theoretical Aspects*, International Journal of Solids and Structures, Vol. 25, No. 7, 803-833, 1989.

[3] Burns, N.H., and Seiss, C.P., *Load-Deformation Characteristics of Beam-Column Connections in Reinforced Concrete*, Civil Engineering Studies, SRS No.234, 1962.

[4] Lubliner, J., Oliver, J., Oller, S., and Oñate, E., *A Plastic-Damage Model for Concrete*, International Journal of Solids and Structures, Vol. 25, No. 3, 299-326, 1989.

[5] Yazdani, S., and Schreyer, H.L., *Combined Plasticity and Damage Mechanics Model for Plain Concrete*, Journal of Engineering Mechanics, Vol. 116, No. 7, 1435-1450, 1990.

[6] Han, D.J., Chen, W.F., *Strain Space Plasticity Formulation for Hardening-Softening Materials with Elastoplastic Coupling*, International Journal of Solids and Structures, Vol. 22, No. 8, 935-950, 1986.

[7] Hughes, T.J.R., and Simo, J.C., *Computational Inelasticity*, Submitted for Publishing, (1997).

[8] Ortiz, M., *A Constitutive Theory for the Inelastic Behavior of Concrete*, Mechanic of Materials, 4, 67-93, 1985.

[9] Bresler, B. and Scordelis, A.C., *Shear Strength of Reinforced Concrete Beams*, Journal of the American Concrete Institute, 60, 51-72, 1963.

[10] Kupfer, H. and Hilsdorf, H.K., *Behavior of Concrete Under Biaxial Stress States*, ACO MAterials Journal, 228-236, August 1969.

[11] MacGregor, J.G., *Reinforced Concrete Mechanics and Design*, Prentice Hall, 1992.

[12] Gerstle, K.H., et. al. *Strength of Concrete Under Multiaxial Stress States*, ACI Special Publication, Vol. 55, No. 5, 103-131, 1981.

[13] Gurtin, *An Introduction to Continuum Mechanics*, Mathematics in Science and Engineering, Vol. 158, 1981.

[14] Kotsovos, M.D. and Newman, J.B., *Mathematical Description of Deformational Behavior of Concrete Under Generalized Stress Beyond Ultimate Strength*, ACI Materials Journal, 340-346, September-October 1980.

[15] Oliver, J., *A Consistent Characteristic Length of Smeared Cracking Models*, International Journal of Numerical Methods in Engineering, 28, 461-474, 1989.

[16] Rashid, Y.R., *Ultimate Strength Analysis of Prestressed Concrete Pressure Vessels*, Nuclear Engineering Design, 7, 334-344, 1968.

[17] Malvar, L.J. and Warren, G.E., *Fracture Energy of Three Point Bend Tests on Single Edge Notched Beams*, Experimental Mechanics, 251-260, 1988.

[18] Simo, J.C., Kennedy, J.G., and Govindjee, S., *Non-Smooth Multisurface Plasticity and Viscoplasticity. Loading and Unloading Conditions and Numerical Algorithms*, International Journal of Numerical Methods in Engineering, 26, 2161-2185, 1988.

[19] Simo, J.C., and Taylor, R.L., *Consistent Tangent Operators for Rate Independent Elastoplasticity*, Computational Methods in Applied Mechanics and Engineering, 48, 101-118, 1986.

[20] Ju and Simo, *Strain and Stress Based Continuum Damage Models – II. Computational Aspects*, International Journal of Solids and Structures, Vol. 23, No. 7, 841-869, 1987.

[21] Lubliner, *Plasticity Theory*, Macmillan Publishing Co., 1990.

[22] Yin, W.S., et. al., *Biaxial Tests of Plain and Fiber Concrete*, ACI Materials Journal, Vol 88, 181-185, March-April 1991.

A Consistent Tangent

Due to the length of the expressions, a simplified notation is adopted. First, define

$$\Xi^{-1} = \mathcal{D}^n + \Delta\gamma_4\phi_{4,\sigma\sigma}$$

Then, using matrix notation define g and d:

$$g = \begin{bmatrix} \phi_{1,\sigma} : \Xi : \phi_{1,\sigma} - \phi_{1,\gamma_1} + \frac{\eta}{\Delta t} & \phi_{1,\sigma} : \Xi : \phi_{2,\sigma} - \phi_{1,\gamma_2} & \phi_{1,\sigma} : \Xi : \phi_{3,\sigma} - \phi_{1,\gamma_3} & \phi_{1,\sigma} : \Xi : \phi_{4,\sigma} \\ \phi_{2,\sigma} : \Xi : \phi_{1,\sigma} - \phi_{2,\gamma_1} & \phi_{2,\sigma} : \Xi : \phi_{2,\sigma} - \phi_{2,\gamma_2} + \frac{\eta}{\Delta t} & \phi_{2,\sigma} : \Xi : \phi_{3,\sigma} - \phi_{2,\gamma_3} & \phi_{2,\sigma} : \Xi : \phi_{4,\sigma} \\ \phi_{3,\sigma} : \Xi : \phi_{1,\sigma} - \phi_{3,\gamma_1} & \phi_{3,\sigma} : \Xi : \phi_{2,\sigma} - \phi_{3,\gamma_2} & \phi_{3,\sigma} : \Xi : \phi_{3,\sigma} - \phi_{3,\gamma_3} + \frac{\eta}{\Delta t} & \phi_{3,\sigma} : \Xi : \phi_{4,\sigma} \\ \phi_{4,\sigma} : \Xi : \phi_{1,\sigma} & \phi_{4,\sigma} : \Xi : \phi_{2,\sigma} & \phi_{4,\sigma} : \Xi : \phi_{3,\sigma} & \phi_{4,\sigma} : \Xi : \phi_{4,\sigma} - \phi_{4,\gamma_4} \end{bmatrix}$$

$$d = \begin{bmatrix} \Xi : \phi_{1,\sigma} & \Xi : \phi_{2,\sigma} & \Xi : \phi_{3,\sigma} & \Xi : \phi_{4,\sigma} \end{bmatrix}$$

With these definitions the algorithmic tangent is given by:

$$\mathcal{C}_{ALG}^{n+1} = \Xi - \{d\}[g]^{-1}\{d\}^T$$

where it is implied that the stress and consistency parameters used to compute the tangent are the converged values at time t^{n+1}. When not all surfaces are active one merely deletes the inactive rows and columns to obtain the appropriate expression.
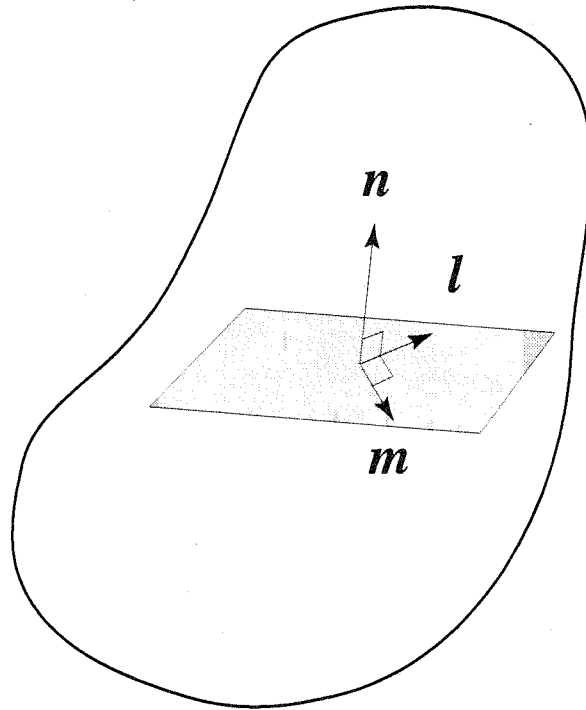
Figure 1: Crack plane orientation. The vectors m and l form the basis for the shear plane; n defines the crack normal or direction of opening.
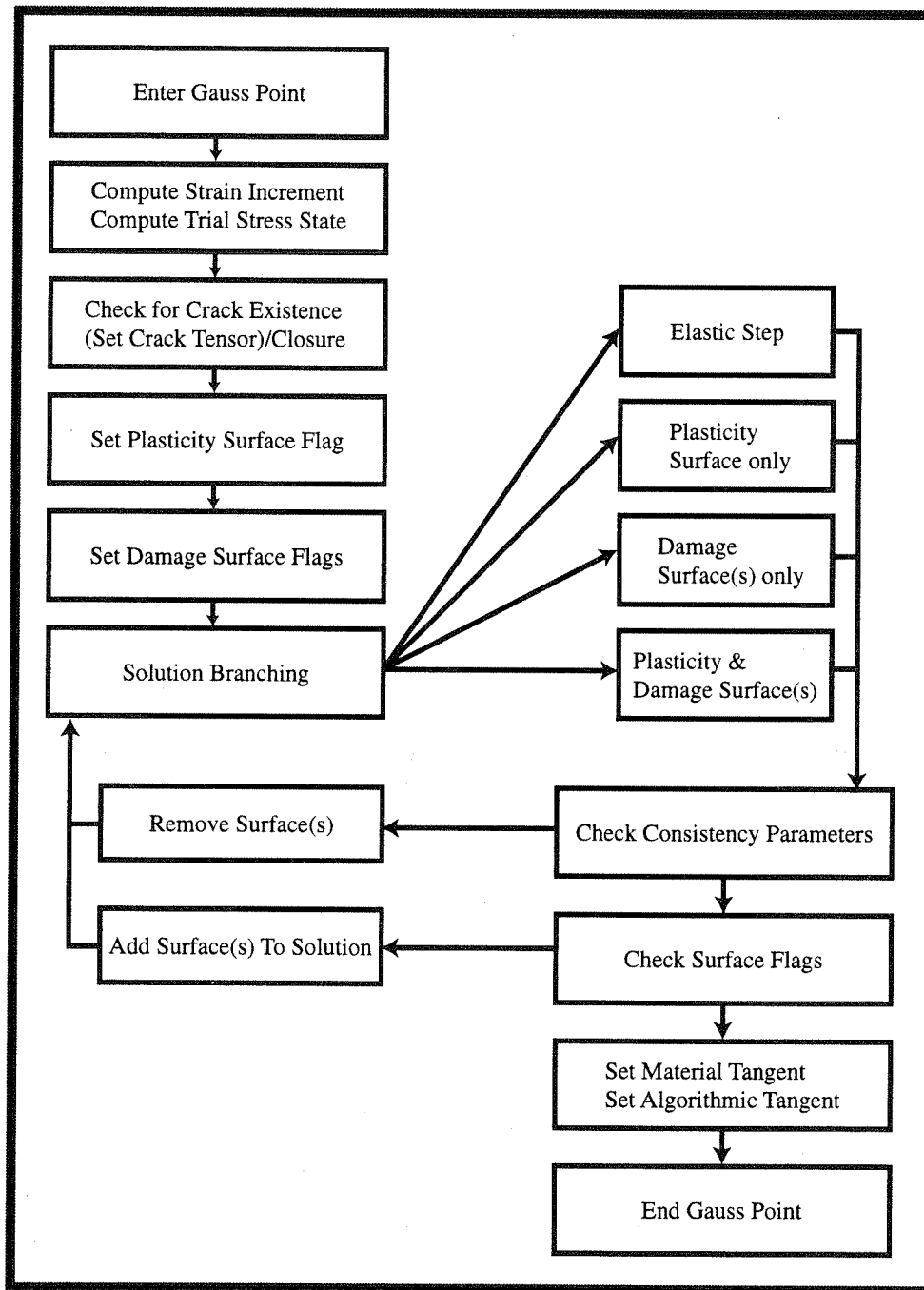
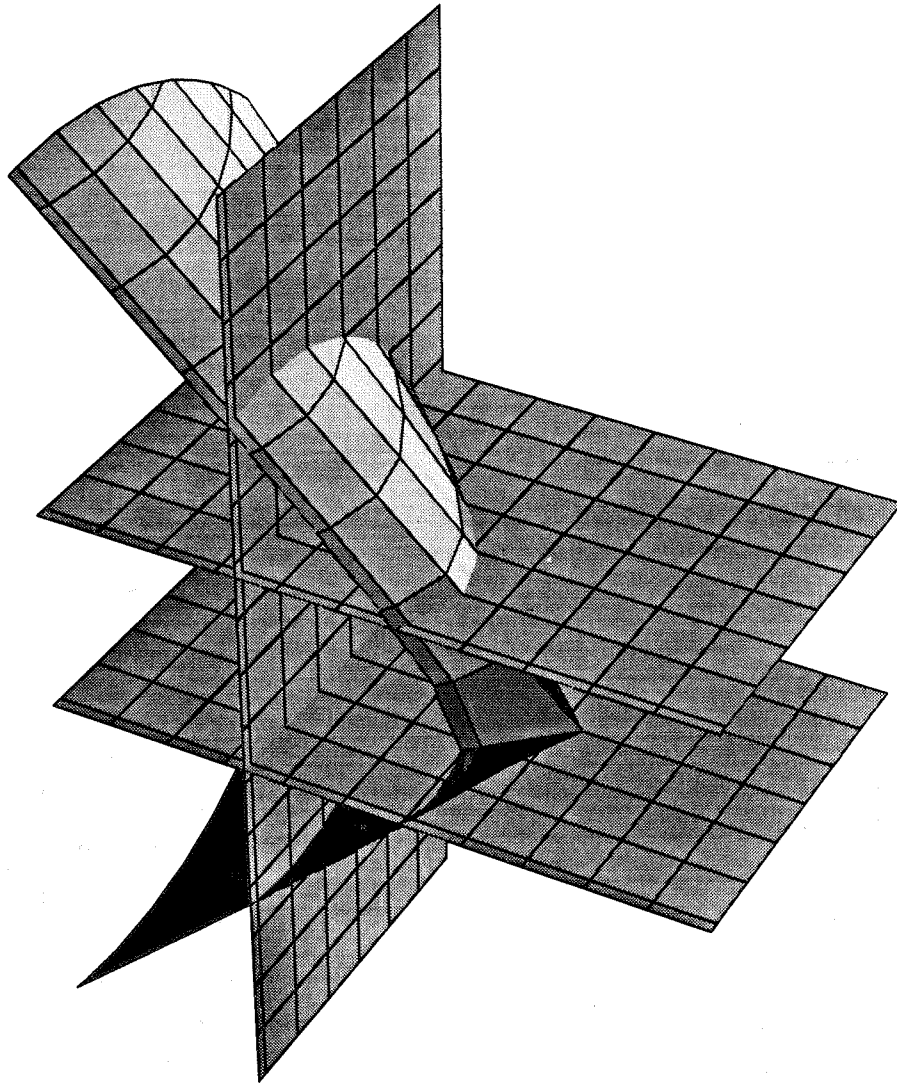Figure 2: Schematic of the Solution Algorithm.

Figure 3: Stress subspace showing the non-smooth intersection between plasticity and damage surfaces following crack formation. The axis of the plasticity cone is a measure of hydrostatic pressure, while distances in the orthogonal plane indicate changes in shear stress. The elastic domain is contained in the boxed off region to the left (from this particular vantage point in stress space).
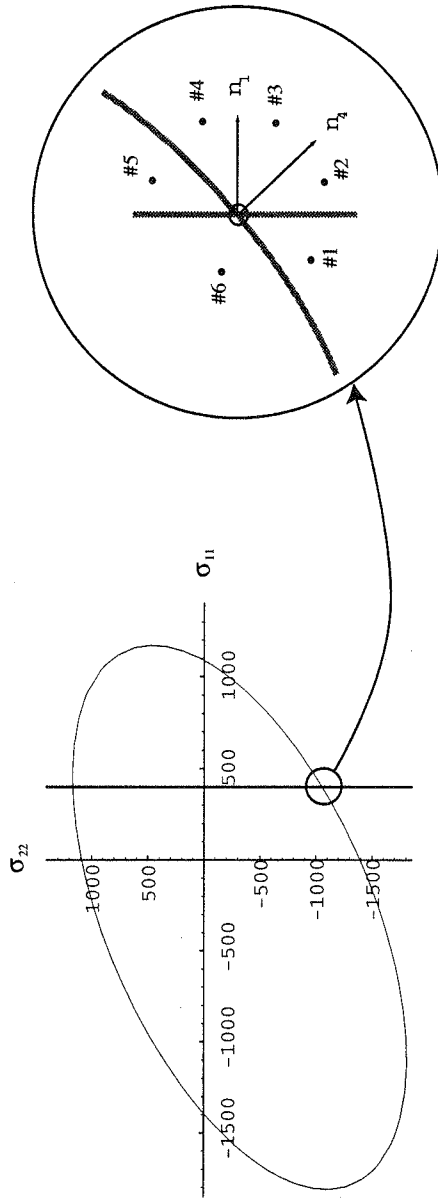
Figure 4: Projection of plasticity surface and tensile damage surface on biaxial stress plane following crack formation. By considering the surface normals, shown by the arrows, six distinct regions in this subplane are created, and four different initial sets of active surfaces (s_{active}) are possible.
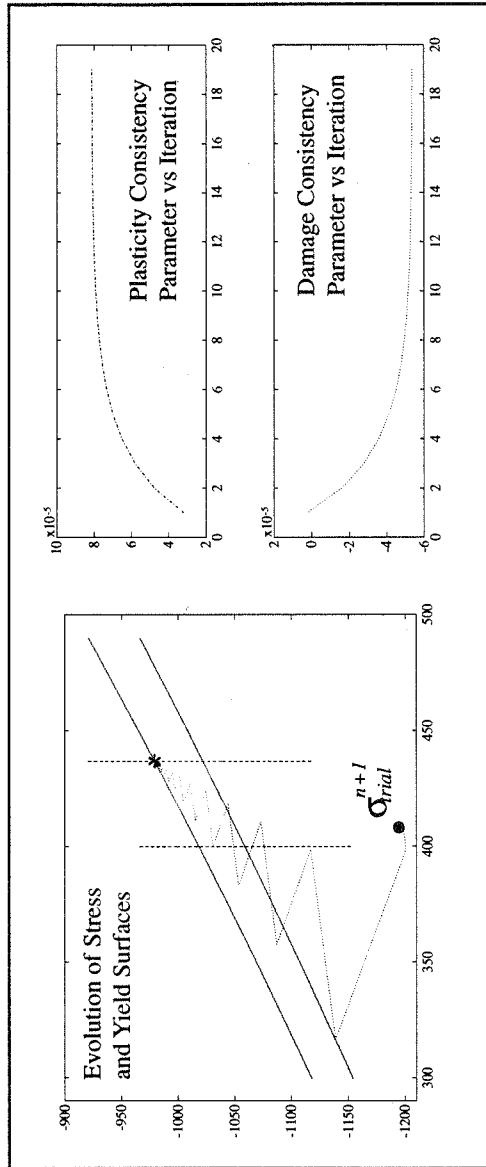
Figure 5: Convergence if the proposed algorithm in region two of Figure 4. The initial starting point is marked by • and labeled as σ_{trial}^{n+1}. The ending point and final surfaces are located by the symbol *, while the initial surfaces are unmarked. After determining a negative $\Delta\gamma_4$, the correct solution consisting of only the plasticity surface is found next.
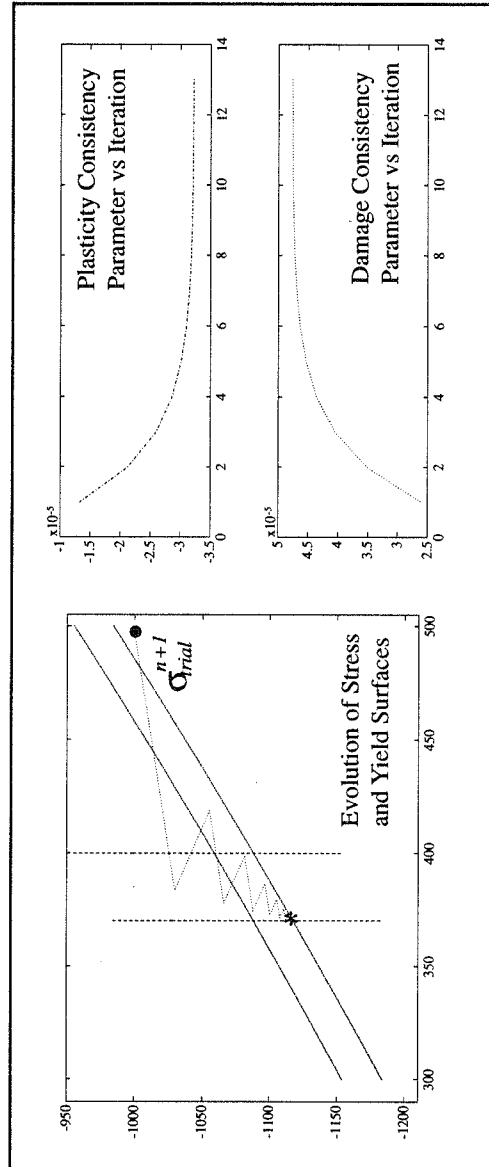
Figure 6: Convergence from region four (refer to Figure 4). The initial starting point is marked by ● and labeled as σ_{trial}^{n+1}. The ending point and final surfaces are located by the symbol ∗, while the initial surfaces are unmarked. In this case, the plasticity surface does not belong to the active set, as indicated by the negative consistency variable.
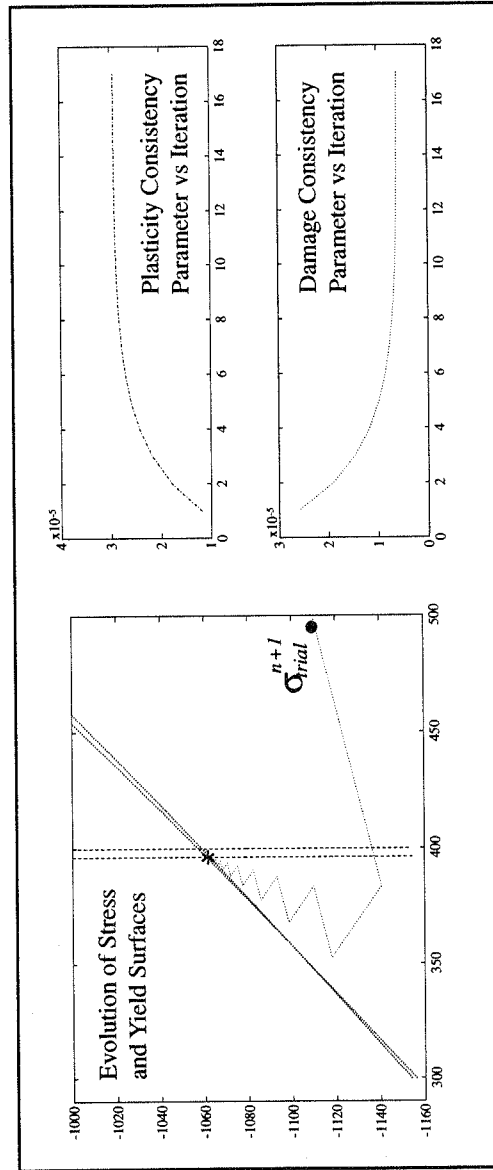
Figure 7: Convergence to a state in which the correct active set includes damage and plasticity surfaces. The initial starting point is marked by ● and labeled as σ_{trial}^{n+1}. The ending point and final surfaces are located by the symbol *, while the initial surfaces are unmarked. The initial stress state was in region three of Figure 4.
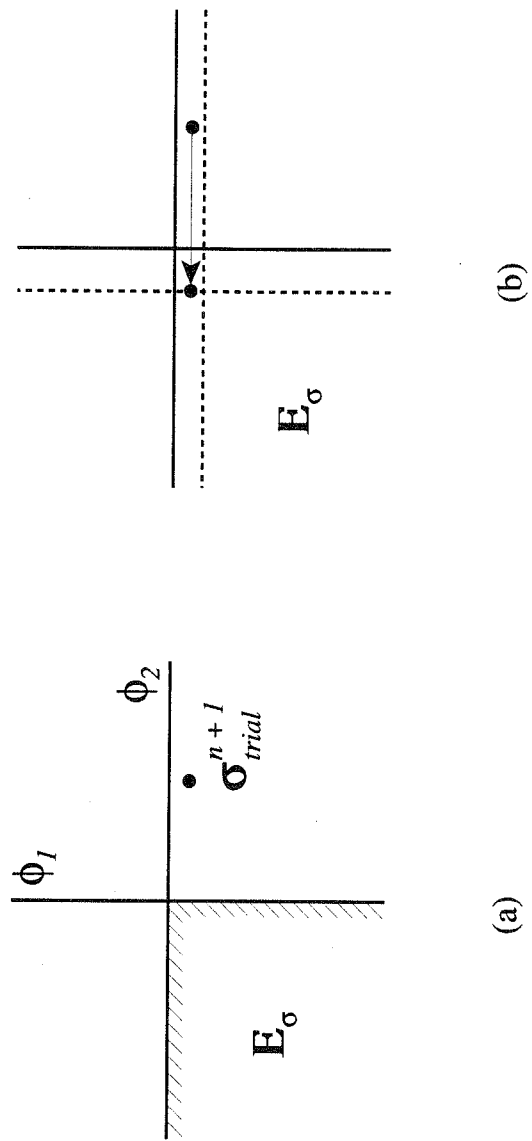
Figure 8: Evolution of the "inactive" surface ϕ_2. This simple example illustrates how a surface may be added to the active set.
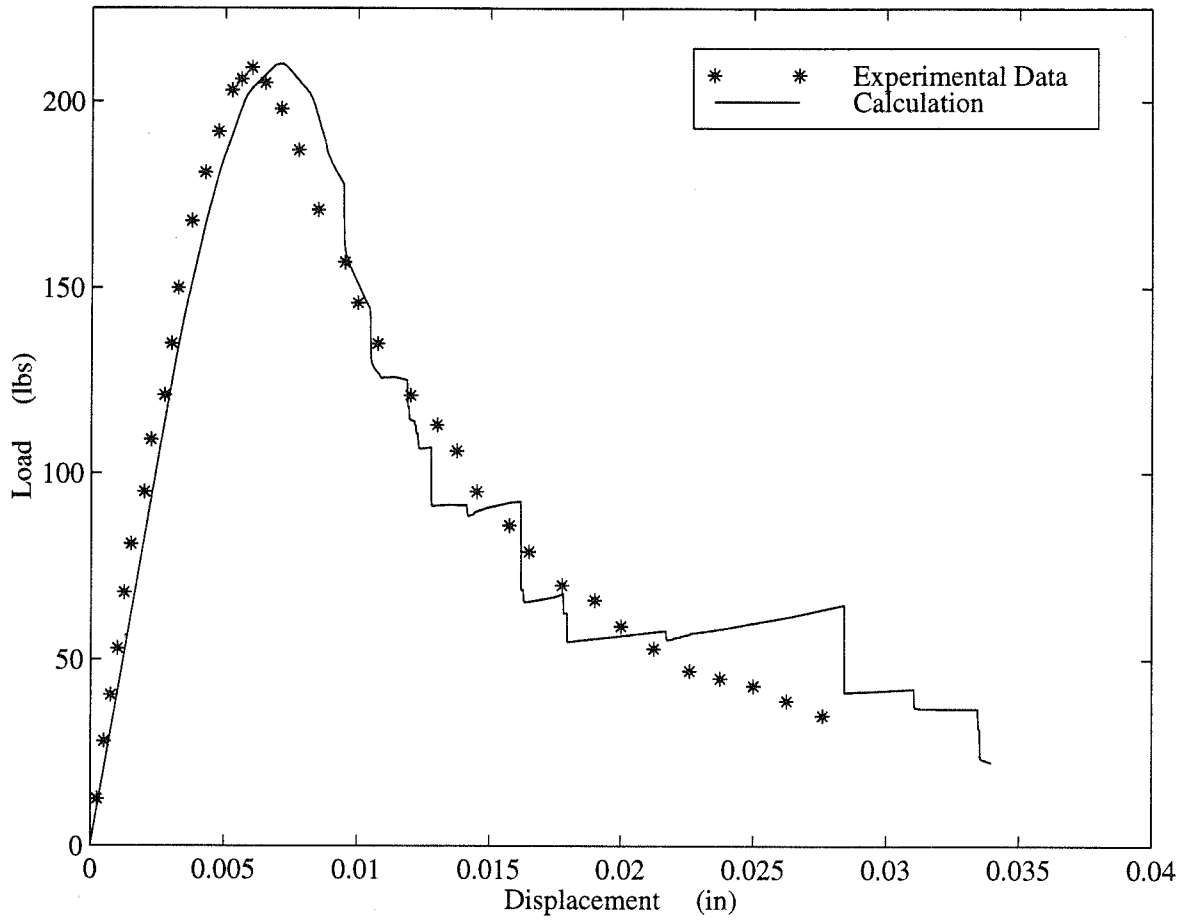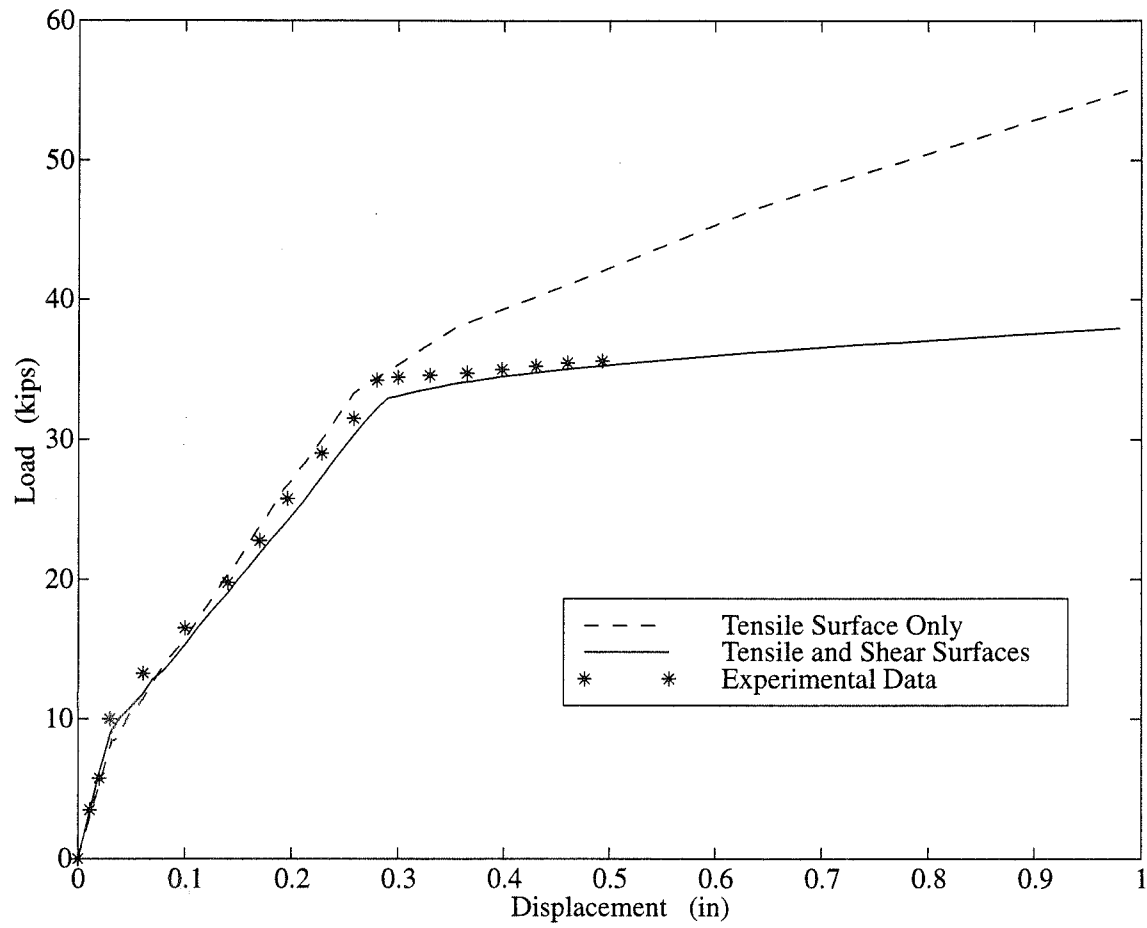
Figure 9: Beam 1B calculation results.

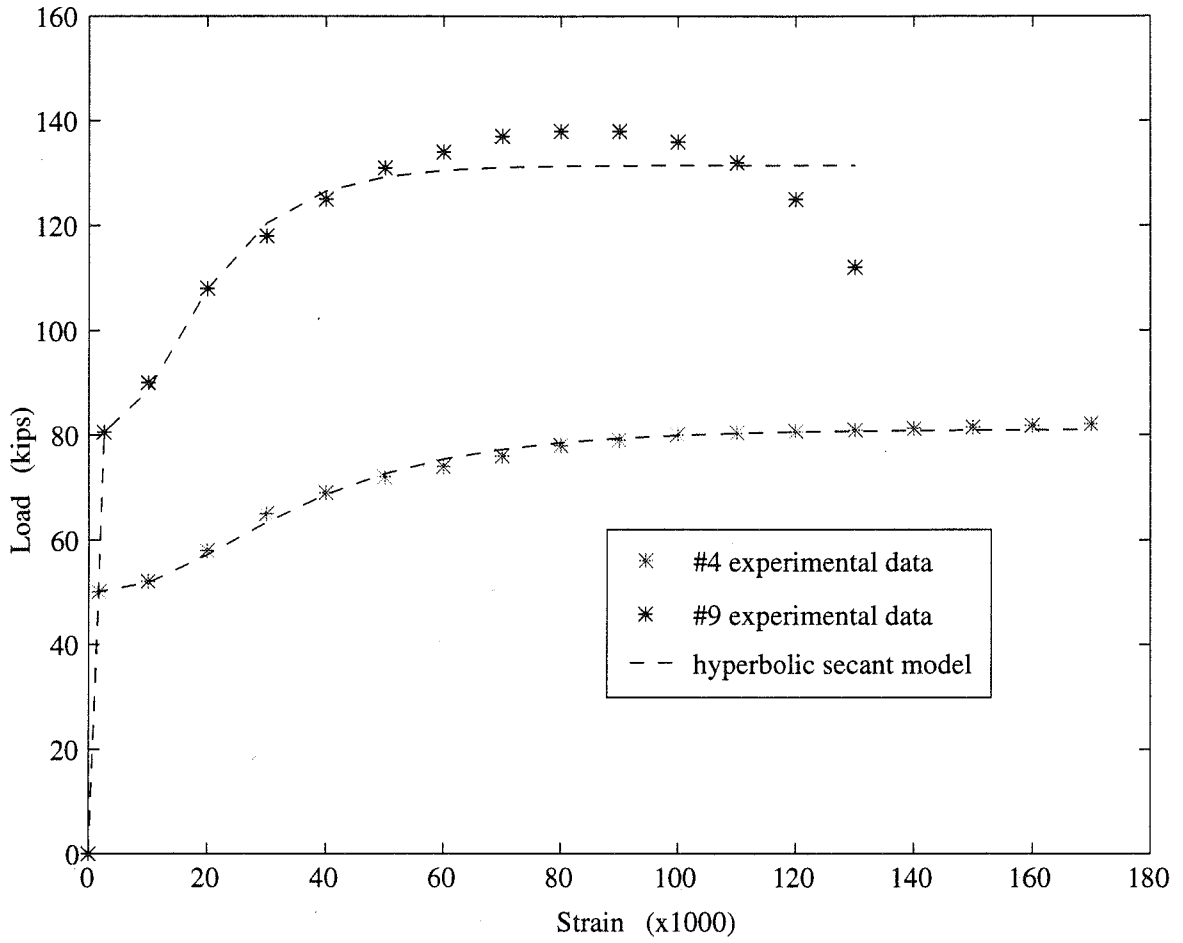Figure 10: Beam J4 calculation results.
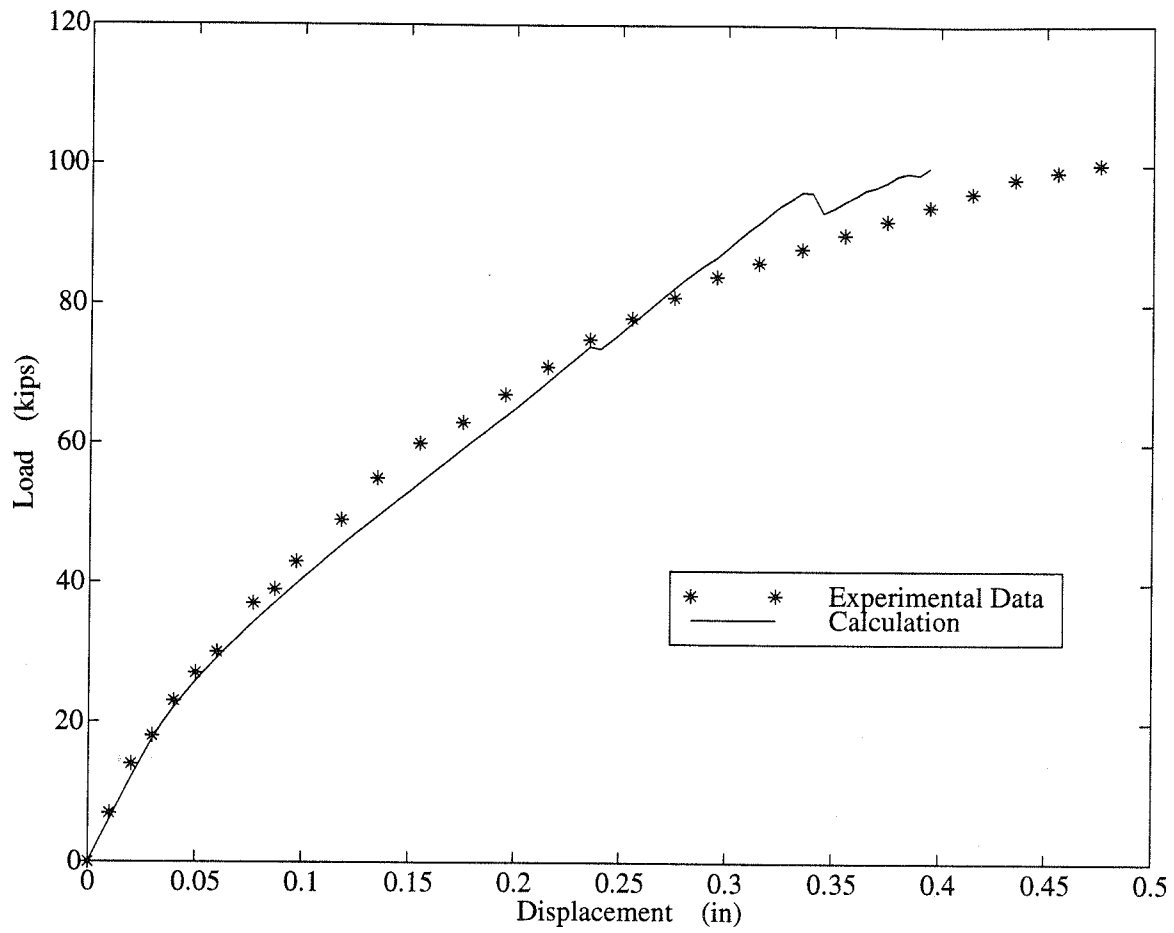
Figure 11: Rebar model used in calculation for Beam A1.

Figure 12: Beam A1 calculation results.